

## A MAP OF THE COSMIC MICROWAVE BACKGROUND FROM THE BEAST EXPERIMENT

PETER R. MEINHOLD,<sup>1,2,3</sup> MARCO BERSANELLI,<sup>4</sup> JEFFREY CHILDERS,<sup>1,3</sup> NEWTON FIGUEIREDO,<sup>5</sup> TODD C. GAIER,<sup>6</sup>  
DORON HALEVI,<sup>1,3</sup> GREGORY G. HUEY,<sup>7,8</sup> MIKKA KANGAS,<sup>1,3</sup> CHARLES R. LAWRENCE,<sup>6</sup> ALAN LEVY,<sup>1,2,3</sup>  
PHILIP M. LUBIN,<sup>1,2,3</sup> MARCO MALASPINA,<sup>9</sup> NAZZARENO MANDOLESI,<sup>9</sup> JOSHUA MARVIL,<sup>1,3</sup> JORGE MEJÍA,<sup>10</sup>  
PAOLO NATOLI,<sup>11</sup> IAN O'DWYER,<sup>7</sup> HUGH O'NEILL,<sup>1,3</sup> SHANE PARENDO,<sup>1</sup> AGENOR PINA,<sup>5</sup>  
MICHAEL D. SEIFFERT,<sup>6</sup> NATHAN C. STEBOR,<sup>1,2,3</sup> CAMILO TELLO,<sup>10</sup> FABRIZIO VILLA,<sup>9</sup>  
THYRSO VILLELA,<sup>10</sup> LAWRENCE A. WADE,<sup>6,12</sup> BENJAMIN D. WANDEL,<sup>7,8</sup>  
BRIAN WILLIAMS,<sup>1,2,3</sup> AND CARLOS ALEXANDRE WUENSCHÉ<sup>10</sup>

Received 2003 March 2; accepted 2004 March 24

### ABSTRACT

We present the first sky maps from the BEAST (Background Emission Anisotropy Scanning Telescope) experiment. BEAST consists of a 2.2 m off-axis Gregorian telescope fed by a cryogenic millimeter wavelength focal plane currently consisting of six Q band (40 GHz) and two Ka band (30 GHz) scalar feed horns feeding cryogenic HEMT amplifiers. Data were collected from two balloon-borne flights in 2000, followed by a lengthy ground observing campaign from the 3.8 km altitude University of California White Mountain Research Station. This paper reports the initial results from the ground-based observations. The instrument produced an annular map covering the sky over  $33^\circ < \delta < 42^\circ$ . The maps cover an area of 2470 deg<sup>2</sup> with an effective resolution of 23' FWHM at 40 GHz and 30' at 30 GHz. The map rms (smoothed to 30' and excluding Galactic foregrounds) is  $57 \pm 5 \mu\text{K}$  (Rayleigh-Jeans) at 40 GHz. Comparison with the instrument noise and correcting for 5% atmospheric attenuation gives a cosmic signal rms contribution of  $29 \pm 3 \mu\text{K}$  (R-J) or  $30 \pm 3 \mu\text{K}$  relative to a Planck blackbody of 2.7 K. An estimate of the actual cosmic microwave background (CMB) sky signal requires taking into account the  $l$  space filter function of our experiment and analysis techniques, carried out in a companion paper. In addition to the robust detection of CMB anisotropies, we find a strong correlation between small portions of our maps and features in recent  $H\alpha$  maps. In this work we describe the data set and analysis techniques leading to the maps, including data selection, filtering, pointing reconstruction, mapmaking algorithms, and systematic effects.

*Subject headings:* cosmic microwave background — cosmology: observations

*Online material:* color figure

### 1. INTRODUCTION

The cosmic microwave background (CMB), interpreted as relic radiation from an early hot dense phase of the universe, is generally acknowledged to be one of the primary probes of conditions in the early universe (Hu & Dodelson 2002 and references therein). Mapping the temperature anisotropies of the CMB has been the subject of intensive effort over the past two decades, with the results of many studies published within the last 3 years: BOOMERANG (Netterfield et al. 2002), MAXIMA (Lee et al.

2001), CBI (Mason et al. 2003), DASI (Halverson et al. 2002), Archeops (Benoit et al. 2002), and ACBAR (Kuo et al. 2004) among others (see Bersanelli et al. 2002 for a recent review). 2003 saw the publication of a large set of papers presenting and analyzing the superb *WMAP* (*Wilkinson Microwave Anisotropy Probe*) data set (Bennet et al. 2003 and references therein), which to a large extent confirmed and extended the previous results.

Temperature anisotropy measurements have been used to calibrate the amplitude of the initial density perturbations and constrain the primordial spectral index (Gorski et al. 1996), to measure the overall density of the universe (De Bernardis et al. 2000, etc.), and recently to make detailed comparisons between competing scenarios for structure formation, leaving a rather narrow range of consistent adiabatic inflationary models. In combination with recent constraints from Type Ia supernovae and large scale structure (LSS) data, CMB temperature anisotropy data strongly suggest models with a large fraction of the total energy density in a cosmological constant or other dark energy (Spergel et al. 2003).

CMB data are normally reduced to an estimate of the angular power spectrum of fluctuations for comparison to theoretical predictions. The salient features of the currently allowed adiabatic inflationary models are a series of “acoustic” peaks and troughs in the power spectrum from  $l$  (spherical harmonic multipole) of about 200 and up (Bond & Efstathiou 1987). The positions and amplitudes of these peaks pin down the details of the cosmological models. Each of the aforementioned experiments was designed to target a particular region of “ $l$ -space”

<sup>1</sup> Physics Department, University of California, Santa Barbara, CA 93106.

<sup>2</sup> University of California, White Mountain Research Station, CA 93514.

<sup>3</sup> University of California—Santa Barbara Center for High Altitude Astrophysics at White Mountain, Santa Barbara, CA 93106.

<sup>4</sup> University of Milano, via Celoria 16, 20133 Milano, Italy.

<sup>5</sup> Universidade Federal de Itajubá Departamento de Física e Química Caixa Postal 50 37500-903—Itajubá, MG, Brazil.

<sup>6</sup> Jet Propulsion Laboratory, California Institute of Technology, Oak Grove Drive, Pasadena, CA 91109.

<sup>7</sup> Department of Astronomy, University of Illinois at Urbana-Champaign, Urbana, IL 61801.

<sup>8</sup> Department of Physics, University of Illinois at Urbana-Champaign, Urbana, IL 61801.

<sup>9</sup> IASF-CNR sezione di Bologna, via P. Gobetti, 101, 40129 Bologna, Italy.

<sup>10</sup> Instituto Nacional de Pesquisas Espaciais Divisão de Astrofísica Caixa Postal 515, 12210-070—São José dos Campos, SP, Brazil.

<sup>11</sup> Dipartimento di Fisica e sezione INFN, Università di Roma “Tor Vergata,” Rome, Italy.

<sup>12</sup> Department of Applied Physics, California Institute of Technology, Pasadena, CA 91125.

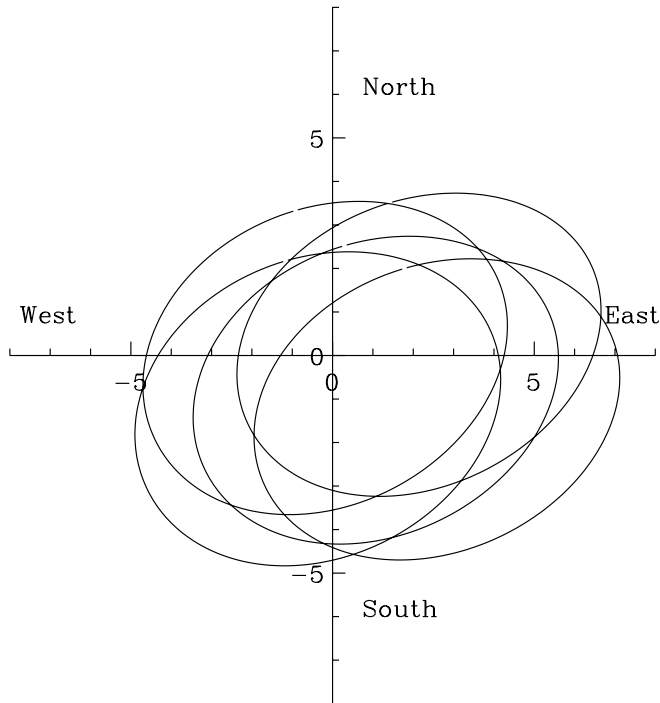


FIG. 1.—Trajectories of the BEAST main beams. The figure is a polar plot about the local zenith. We subdivide the path of each beam into 250 optical “sectors” parameterized by the phase angle of the flat mirror, which spins at about 2 Hz.

or portion of the angular power spectrum. Sensitivity to high  $l$  modes is limited by the angular resolution of the telescope. Resolution in  $l$ -space is limited by the size of the region studied. Amplitude uncertainties at all  $l$  are limited by the detector noise and integration time. At low  $l$ -values in particular, sample variance can increase the amplitude uncertainty of a measurement, an effect that can only be reduced by increasing sky coverage. BEAST, in particular the observing campaign described in this paper, has been optimized to study the first of these peaks in detail.

### 1.1. Instrument Overview

BEAST is a mixed Q-band (38–45 GHz) and Ka-band (25–35 GHz) focal plane that views the sky through a 2.2 m off-axis telescope followed by a modulating flat mirror. Primarily funded by NASA, BEAST is the largest aperture CMB telescope flown to date. The instrument is described in detail in Childers et al. (2005), and the optical design is described in Figueiredo et al. (2005). BEAST is most similar to one of our previous balloon-borne telescopes, HACME (Staren et al. 2000; Tegmark et al. 2000), but with a much larger telescope and a focal plane array. After two balloon flights in 2000, BEAST was reconfigured to take advantage of the University of California White Mountain Research Station (WMRS) site on Barcroft mountain, CA (altitude 3800 m). The data described here were taken with six elements of the array operational, two Ka-band and four Q-band detectors. Two of the Q-band detectors are installed on an ortho-mode transducer (OMT) using a single horn split into vertical and horizontal polarizations. The other horns have single polarization receivers, oriented at various angles. The telescope was installed in an unused building, modified so the roof can be rolled off. BEAST is aligned at  $74^\circ$  east of north and can view nominal central elevation angles from  $60^\circ$  to greater than  $90^\circ$ . The instrument was fully installed and operational at

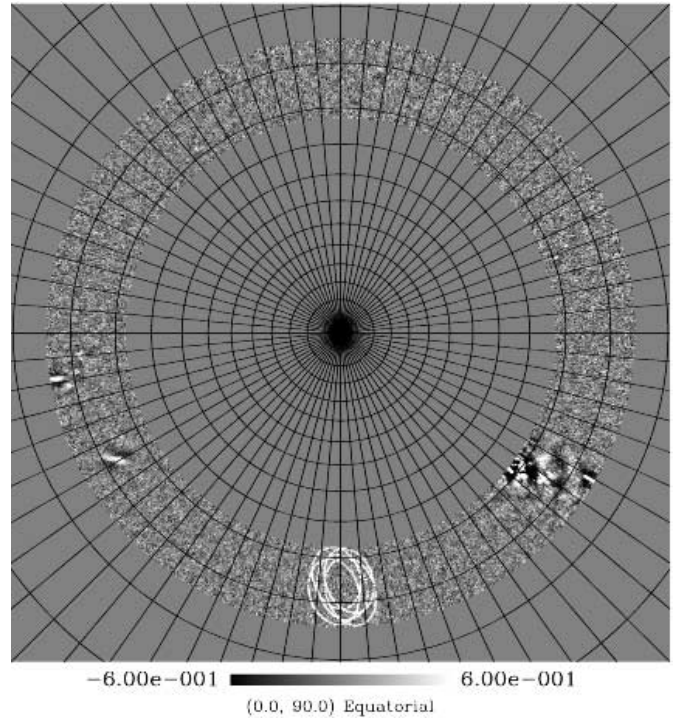


FIG. 2.—BEAST combined Q-band map. The figure is a gnomonic projection about the north celestial pole. The grid lines are  $5^\circ$  in declination and  $5^\circ$  in right ascension. Gray-scale units are mK Rayleigh-Jeans. The trajectories of the 5 beams during 1 revolution of the flat mirror are overlaid on the figure near  $\alpha = 0^\circ$  to illustrate the observing strategy. The flat spins at about 2 Hz; the map includes data from over 4 million flat revolutions. Two Galactic plane crossings are clearly visible on the plot, the brighter around  $\alpha = 20$  hr. Also visible is the large structure at  $\alpha \approx 60^\circ$  found to be due to free-free emission (see the text).

Barcroft in 2001 July and took data nearly continuously until 2001 December. Two more weeks of data were obtained in 2002 February, and a longer campaign took place from 2002 August through October.

### 1.2. Observing Strategy

BEAST views the sky through a large (2.5 m diameter) spinning flat mirror, tilted  $2.2^\circ$  from its rotation axis. As the flat spins this tilt moves the field of view of the telescope around a nearly elliptical path on the sky of diameter about  $9^\circ$ . The five operational feeds thus follow the path shown in Figure 1 for the normal telescope elevation angle of  $90.4^\circ$ . Two main strategies were employed in taking data. The first involved scanning the nominal (central) elevation of the telescope from  $80^\circ$  to  $90^\circ$  and back continuously; the second method was to keep the elevation angle fixed near  $90^\circ$  and allow Earth rotation to provide the mapping scan. All of the data reported here are from the “fixed elevation” data set. This choice was made primarily for the simpler and more robust pointing solution obtained in fixed elevation mode, and the fact that there were no significant improvements in systematic tests gained from the elevation scans. The resulting map is an annulus around the north celestial pole (NCP) of width  $\sim 10^\circ$ , around declination  $37^\circ$ . Figure 2 shows the entire Q-band map with the beam trajectories overlaid.

The output of each radiometer is amplified, AC coupled with a high-pass filter time constant of 15 s, and then integrated in an “ideal” or box-car integrator with nearly 100% duty cycle. The integration time is set for 800  $\mu$ s and digitized to 16 bits.

The angular position of the flat mirror (rotating at 2 Hz) is measured simultaneously so the data can be synchronized with

the instantaneous position of the relevant telescope beam. The first step of analysis involves rebinning the raw 1250 Hz data stream into “optical sectors,” corresponding to 250 angular positions of the flat mirror. Each optical sector therefore identifies an angular position of the flat, which is related by the telescope geometry to a precise azimuth-elevation pointing for each of the five active detector elements. These pointing data are converted to celestial coordinates and then ultimately to HEALPix (Hierarchical Equal Area isoLatitude Pixelisation; Górski et al. 1998) pixel numbers. The resulting optical sector data stream has an effective sampling rate of 450 Hz. The raw data amount to 3.7 Gbytes per day.

### 1.3. Calibration

The receivers are calibrated hourly by passing an ambient temperature microwave absorber between the feeds and the secondary mirror. The output of the acquisition system is then corrected for the effects of the AC coupling in addition to a small (order 10%) correction for compression of the detector outputs while viewing the ambient target. The difference between the load and the sky temperatures is then used to compute the calibration coefficients, measured in  $\text{K V}^{-1}$ . This hourly calibration constant is applied to the data during pipeline analysis. Calibration and effective beam size were confirmed independently using Cygnus A as the celestial source. Overall calibration uncertainty is  $\pm 10\%$  (temperature). Calibration and beam size issues are covered more completely in Childers et al. (2005).

## 2. DATA SET

### 2.1. Raw Data Statistics

Figure 3 shows a sample section of time-ordered data for a typical channel. The top strip of small points is the raw data stream, including electrical and any radiometric offset. The large nearly sinusoidal component is due to the varying atmospheric contribution as the flat sends the beam through different elevations and therefore different optical depths. This variation is approximately 60 mK peak-to-peak for this Q-band (38–45 GHz) channel. We obtain a high signal-to-noise estimate of the nearly constant atmospheric contribution for each revolution by binning all the data for each hour by optical sector to produce

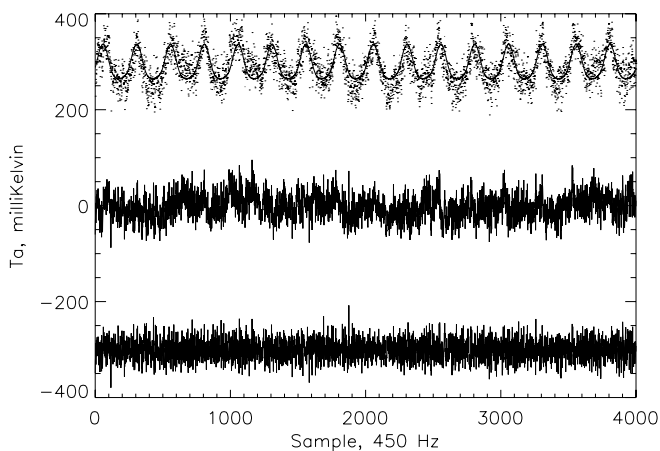


FIG. 3.—Sample of time-ordered data ( $\approx 8$  s). The top strip of small points is the raw data stream. The solid line through the points is the flat synchronous atmospheric template obtained by averaging over this hour (see the text). The central strip of data points clustered near zero are the residuals from the template subtraction. The lower strip of data points show the result of high-pass filtering the template-removed data set at 10 Hz, offset from zero for clarity.

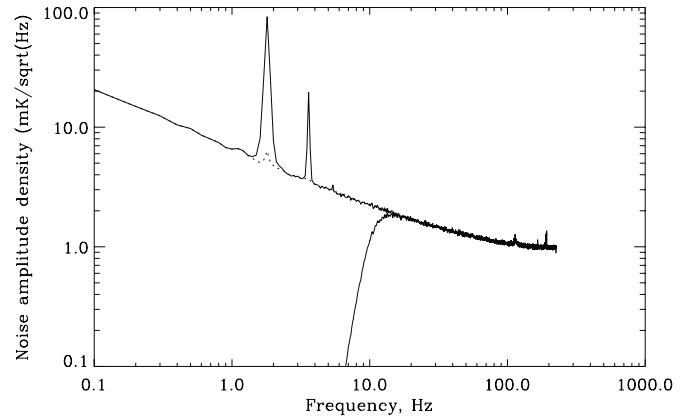


FIG. 4.—Noise amplitude density spectrum from a sample hour of data. The white-noise limit at high frequency, the large  $1/f$  component, the atmospheric signal at the spin rate and its harmonics, and excess noise at 120 Hz are all evident. The noise spectrum for the template-subtracted data (dotted line), and the spectrum after 10 Hz high-pass are plotted as well (dashed line).

a “template” signal for that hour. We then subtract this template from every revolution in that hour to remove the first-order atmospheric contribution. Note that systematic errors fixed in the telescope frame or phase-locked to the flat revolution would be removed as well. Examples of such effects are fixed sidelobe contamination and electrical noise synchronous with the flat motion. Since our strategy keeps the telescope fixed, in principle any sidelobe illumination of the observatory or ground would be removed. There is no direct evidence for any contribution except atmosphere. The solid line plotted through the raw data points is the template for this hour, while the central strip of data points clustered near zero are the residuals from the template subtraction. The lower strip of data points show the result of high-pass filtering the template-removed data set at 10 Hz corresponding to about  $6^\circ$  on the sky (effectively giving us a low  $l$ -space cutoff). These data have been offset from zero for clarity. The combination of 1 hour template removal and steep 10 Hz high-pass filter is a reasonable compromise between extending the low  $l$  coverage and minimizing the increasing effects of  $1/f$  instrument and atmospheric noise contributions. Several other filter cutoffs and filter types have been previously investigated. Without the template removal, harmonics of the spin rate remain in the data and can show up as striping in the maps. Hourly sections of data are our natural units since calibrations happen on the hour, breaking the continuity of the data stream. There appears to be no benefit to using longer sections for calculating the template; we have not yet investigated in detail the advantages of using shorter time periods for template subtraction. Both hourly template removal and 10 Hz high-pass filter were used in the analysis described below.

Estimates for the noise amplitude spectral density for this hour are given in Figure 4, calibrated in  $\mu\text{K} \sqrt{\text{Hz}}^{-1}$ . The large signal near 2 Hz and its higher frequency harmonics are due to the atmospheric contribution discussed above. Note that because the beam trajectory is not circular, and passes beyond zenith, the resulting atmospheric signal is distorted from sinusoidal, producing significant harmonics of the spin frequency. Also shown on the plot is the noise density after template removal and 10 Hz high-pass filtering. The plot demonstrates the BEAST detector noise has significant contributions from correlated, long memory (or “ $1/f$ ”) noise. The knee frequency of  $1/f$  noise is defined as the frequency at which the total noise power spectral density ( $1/f$  + white) exceeds by a factor of 2 its white-noise

TABLE 1  
SUMMARY STATISTICS FOR A TYPICAL HOUR OF SKY DATA

Channel	Frequency (GHz)	White Noise ( $\mu\text{K } \sqrt{\text{s}}$ )	1/f Knee (Hz)	Template
				$p$ - $p$ (mK)
2.....	38–45	746	38	90
3.....	38–45	1416	40	159
4.....	38–45	823	60	109
6.....	25–35	1183	105	81.3
7.....	25–35	1033	110	114
8.....	38–45	686	58	93

level. The latter determines our sensitivity per unit time for angular scales near the beam size. Table 1 summarizes the receiver and atmospheric noise and signal performance for a typical accepted hour of data from this campaign.

### 2.2. Pointing Reconstruction

The BEAST scan strategy produces a large area map (2470 deg<sup>2</sup>) with high resolution, and we require a precise pointing solution to associate every optical sector for every channel with a position in celestial coordinates. We know the geometry of the telescope, but not well enough to calculate the beam positions to sufficient accuracy for map reconstruction. Deviation from ideality of the optics gives uncertainties on the a priori knowledge of the beam positions. BEAST was placed in an existing building that did not allow us to move the telescope appreciably in azimuth, and we are unable to target the Moon, Sun, or any planets for pointing verification. We bootstrapped the pointing model by starting with the known geometry, then flying a small airplane equipped with GPS over the system in a grid pattern. The spikes in the BEAST data due to the airplane thermal emission were then correlated with the measured relative position of the airplane to make a crude improvement to the pointing model. Cygnus A as well as several other well-known radio sources are included in our map, and we have been able to use these sources to further refine the pointing model, beam size, and calibration. Figure 5 is a portion of the final map (all Q-band channels averaged) showing Cygnus A and the Cygnus Loop region. The reconstruction returns an effective resolution of  $23' \pm 1'$  FWHM in Q-band. This is in contrast with the previously measured telescope resolution of  $19' \pm 2'$ . The smearing from the design resolution to the measured effective FWHM of  $23'$  is due to a combination of unmeasured pointing errors (telescope flex, long-term telescope sag), residual errors in the pointing reconstruction algorithm, smearing due to the finite HEALPix resolution of  $6'.9$ , and smearing from the initial flat rotation sectors (about  $6'.7$ ). The pointing model is converted to a lookup table of azimuth and elevation for each horn, sector, and telescope elevation for use in the pipeline processing.

### 2.3. Data Reduction and Analysis

The first data reduction step was to reformat the data into optical sectors and incorporate relevant pointing information into a single file (called a level 0 FITS file), which conforms to the FITSIO standard. A single file was produced for each hour, including all channels, as well as telescope elevation, and other pointing information. In addition to rebinning to optical sectors we measured some statistics on these hourly sets to allow simple data culling later. In particular, we measured the rms of

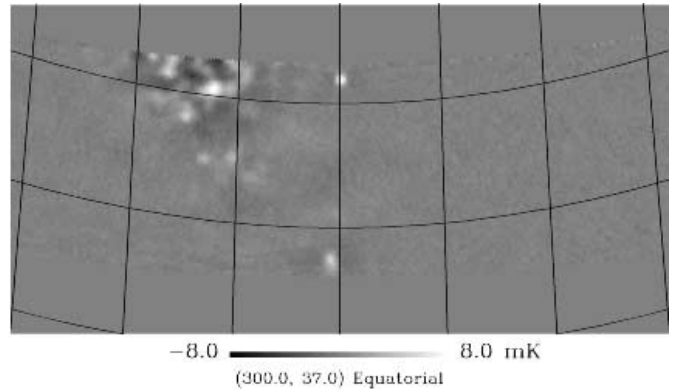


FIG. 5.—Gnomonic projection of the Q-band map near Cygnus A and the Cygnus Loop region. The grid spacing is  $5^\circ$  in right ascension and declination. Cygnus A has been used as a pointing calibration as well as a cross-check of the effective beam size and calibration constant. All of the sources seen here have been identified with known objects.

each channel for the hour as well as the rms after high-pass filtering the data at 10 Hz. Transients (generally due to thermal emission from airplanes crossing the instruments field of view) were removed and replaced with adjacent data. These points were flagged as “unusable” for later analysis stages. Level 0 processing was as follows: (1) import 1 hr receiver and pointing data; (2) calculate statistics (rms and high-pass filtered rms); (3) rebin raw (not high-pass filtered) data to optical sectors; (4) remove transients, flag bad or replaced points; (5) store data to FITS, save summary statistics in header.

The next step was to cull the data for bad weather and out of specification performance (i.e., when systems were off or under test or during calibrations). This was done by looking at the statistics of the high-pass filtered data rms in the level 0 headers. Generally, all the channels showed the same sensitivity to bad weather, and there was a clear knee in the distribution of rms for making the cut.

The total data set for fixed elevation observations includes 1278 hr, measurements made over a total of 84 days at all times of the year. Data culling for bad weather and system irregularities of all kinds brought that down to 682 hr. Of each hour, 10% is spent on calibration. Our “data efficiency” is around 50%. It should be noted that we observed in all but the worst weather, partly to learn as much about the atmospheric effects on the data as possible, and our efficiency is a reasonable measure of conditions at White Mountain generally during our campaigns.

We then moved to level 1 data files, which integrated the pointing data as map pixel indices. We chose to use the HEALPix (Górski et al. 1998) set of standards and routines, partly for the inherent advantages of the pixelization scheme and partly for the extensive infrastructure of tools available from the HEALPix team for manipulating and visualizing the resulting maps. This standardization and set of tools has been invaluable in performing all of our subsequent analysis.<sup>13</sup> Every sample for each channel was then associated with an azimuth-elevation pointing via the lookup table mentioned above, then to a celestial coordinate pointing using the known observation time and location, thence to a HEALPix index using the HEALPix IDL library routines. We use NSIDE = 512, with a resolution corresponding to  $6'.9$  pixels as a reasonable oversampling of our beam size. Level 1 data files

<sup>13</sup> The HEALPix homepage is available at <http://www.eso.org/science/healpix/>.

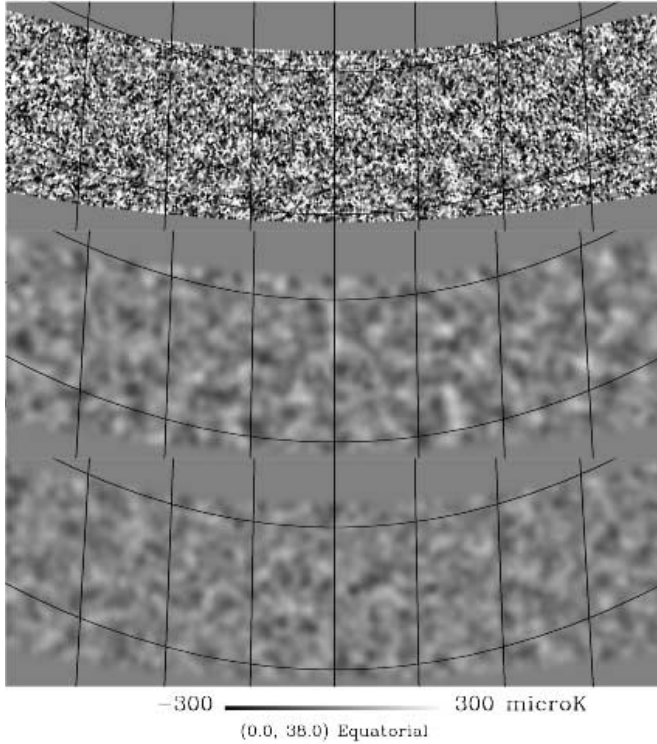


FIG. 6.—Gnomonic projection of the Q-band map centered at  $\alpha = 0^\circ$  and  $\delta = +38^\circ$ . The top map is the full resolution (6.9 pixels) map. The center map is smoothed with a  $30'$  FWHM Gaussian. The bottom map is the first half/second half difference map, also smoothed to  $30'$ . The difference map should have only noise, while the average map (*center*) should show noise+cosmic structure. Declination increases up, right ascension increases to the left, and the grid is  $5^\circ$  spacing in right ascension and  $10^\circ$  in declination.

then include time, six columns of data, one column of “goodness-of-data” flag, and six columns of HEALPix indices.

To produce a map, we (1) read in level 1 file, (2) calculate and subtract hourly atmospheric template from all channels, (3) high-pass filter all channels at 10 Hz, (4) bin into daily map (ignoring flagged points, saving statistics), (5) iterate for all hours to complete daily map for all channels, and (6) save daily map to disk and start next day. This generates a map with statistics for each day for each channel. We then co-added (averaged by pixel) the daily channel maps into total data set channel maps, weighting by the average noise per pixel per day. The Q-band channels were then co-added with appropriate noise weighting to create the total Q-band data maps, as were the Ka channels. In addition to these averaged maps, we made “difference” maps, in which we binned 1/2 of the days into one map, the other 1/2 of the days into another. Then we generated the difference of these two maps on a pixel-by-pixel basis, dividing by 2 to maintain the noise statistics of the average maps. These difference maps give us a measure of the noise in the maps versus the signal+noise in the average maps.

#### 2.4. Maps

Figures 6 and 7 display two representative sections of the BEAST Q-band average map. Each figure contains three panels. The top panel is the full  $N_{\text{side}} = 512$  resolution map in gnomonic projection around  $\delta = 38^\circ$  and  $\alpha = 0$  and  $160^\circ$ . The second panel is this same map smoothed with a  $0.5^\circ$  FWHM Gaussian. The third panel is the  $0.5^\circ$  FWHM smoothed difference map as a visual guide to the effective noise level in the smoothed average map.

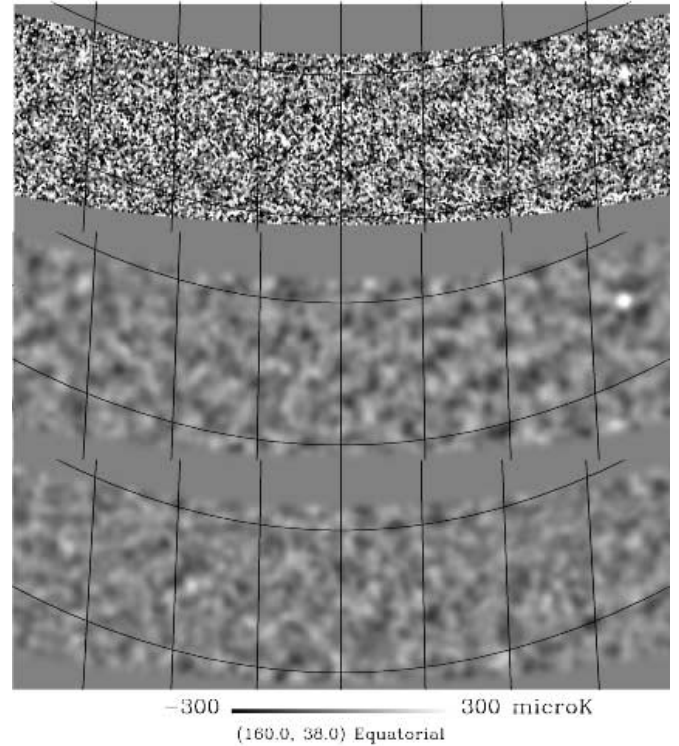


FIG. 7.—Gnomonic projection of the Q-band map centered at  $\alpha = 160^\circ$  and  $\delta = +38^\circ$ . This section of the map has an obvious point source at the upper right (removed for power spectrum analysis).

Figure 8 shows the distribution of pixel values for the Q-band map, compared with a Gaussian distribution. The distributions with and without the Galaxy and point source cuts are shown. There is a clear reduction in outliers, and the remaining points are quite smoothly distributed. The significant “tails” in the Galaxy removed set are due to the nonuniform distribution of integration time. One measure of the noise and signal in the map is to calculate the standard deviation of the map (after removing foreground contaminated regions) and compare with the standard deviation in the difference map, which should have the same noise characteristics, but no CMB signal. For the Q band we find  $270 \pm 27 \mu\text{K}$  at  $6.9$  pixels for the sum map and  $268 \pm 27 \mu\text{K}$  for the difference map. This implies a cosmic signal

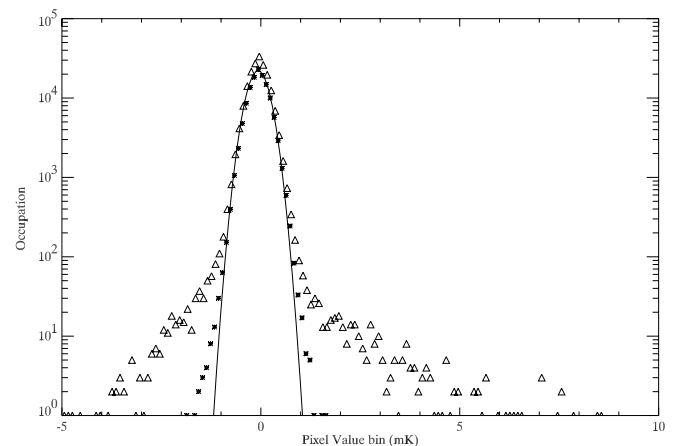


FIG. 8.—Histogram of the full resolution Q-band map pixels. Open triangles are the full map, asterisks are the map with Galaxy ( $|b| < 17.5^\circ$ ), and point sources removed, while the smooth curve is a Gaussian with  $250 \mu\text{K}$   $\sigma$ .

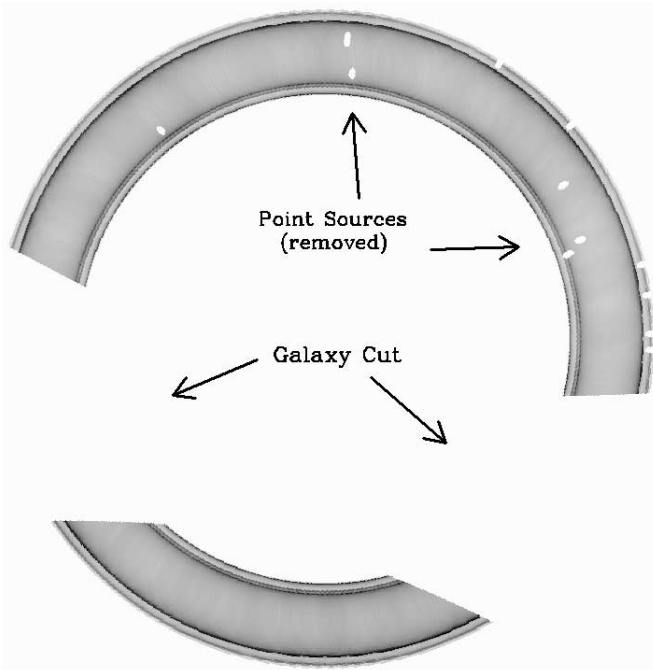


FIG. 9.—Number of 2.2 ms observations per  $6.7'$  pixel for the Q-band channel co-added map. The scale extends from 0 (white) to 60,000 (black). We show the map sections available for power spectrum analysis after foreground cuts ( $|b| < 17.5^\circ$ ), point source removal, and trimming in declination for very uneven sampling.

contribution of  $31 \pm 3 \mu\text{K}$ . Smoothing to  $30'$  FWHM we get  $57 \pm 5 \mu\text{K}$  for the sum and  $49 \pm 5 \mu\text{K}$  for the difference, consistent with a signal rms contribution of  $28 \mu\text{K}$  (Rayleigh-Jeans units). Converting to a blackbody spectrum and correcting for 5% atmospheric attenuation we obtain  $30 \pm 3 \mu\text{K}$  (quoted error dominated by calibration uncertainty). Note that this includes the map smoothing, and the complex BEAST filter produced by our AC coupling, beam shape, high-pass filter, and template removal, so is not our best estimate of cosmic signal, but only an indicator of a statistically significant sky signal.

We compared the full resolution sum and difference maps with the null hypothesis. The  $\chi^2$  of the sum map is 126,620 and the difference map is 124,835 for 124,574 points. These correspond to  $<0.1\%$  and  $>29\%$  probabilities of being consistent with zero, respectively. We have not attempted a careful analysis of the degrees of freedom in these maps, as our power spectrum estimation technique automatically corrects for this. Also the  $\chi^2$  numbers quoted here use the simple pixel errors compiled from the distributions obtained during mapmaking: more sophisticated analyses are possible and would be required to use these numbers for anything more than a “sanity check.”

### 2.5. Foregrounds

Any sensitive CMB map of this size will cross regions of significant foreground contamination, as is seen in our maps with the Galactic crossings. Except for a few regions the map appears to be remarkably clean. By comparison with foreground maps, we have been able to determine a very conservative cut in Galactic latitude that removes diffuse foregrounds, while for point sources we have used a strict point source finding algorithm operating on the data maps. Point sources were removed by excising a  $1^\circ$  diameter circle of pixels centered on each source. The most interesting feature of our foreground contamination is a large structure near  $\alpha = 60^\circ$ ,  $\delta = 36.5^\circ$ . The fea-

ture is 0.75 mK in the smoothed Q-band map and 1.4 mK in Ka-band, implying a power law spectral index of  $-1.9$ , consistent with free-free emission. We see a large correlation with a feature in the “SFD” combined *IRAS* and *DIRBE* map (Schlegel et al. 1998), but no correlation at all with the Haslam map at 408 MHz. Initially, we thought this might be evidence for spinning dust grains, but a comparison with integrated  $H\alpha$  emission showed a very large correlation, consistent with free-free emission. This comparison was made possible by the availability of a map of integrated  $H\alpha$  emission produced by D. Finkbeiner (2003) using data from WHAM (Reynolds et al. 2002), VTSS (Dennison et al. 1998), and SHASSA (Gaustad et al. 2001). The expected free-free emission is estimated by scaling from Bennett et al. (1992), which predicts  $3 \mu\text{K}$  per rayleigh at 40 GHz. For our structure we measure  $5.7 \mu\text{K}$  per rayleigh. The correlations with the  $H\alpha$  map are so much more evident than with Haslam and *IRAS* that we can use the  $H\alpha$  data to estimate our required Galactic latitude cut: by cutting out data with  $|b| < 17.5^\circ$  we expect less than  $10 \mu\text{K}$  contamination from free-free emission. This is a conservative cut, and we could refine this further to increase the accepted sky fraction. A more detailed treatment appears in the companion paper by Mejia et al. (2005), which focuses on foreground estimation from these maps. Our resulting foreground removal template is shown in Figure 9, shaded regions were used in the power spectrum analysis of O’Dwyer et al. (2005).

### 3. DISCUSSION

We have produced extended ( $\sim 2500 \text{ deg}^2$ ) sky maps with good angular resolution and control of systematics. Visual inspection of the smoothed maps shows unmistakable structure. Quantitative results for the power spectrum of CMB fluctuations, which are consistent with our data, are presented in a companion paper (O’Dwyer et al. 2005). In addition to cosmic structures we have interesting correlations with known astrophysical foregrounds. Further analysis will yield important information about the amplitude, spectra and possibly polarization of these foregrounds.

Accurate power spectra from the data calculated using a MASTER-like algorithm (Hivon et al. 2002), and cosmological parameter estimates are presented in a companion paper (O’Dwyer et al. 2005). In addition, however, in iterating our filters, template removal, and other mapmaking steps, we devised a fast tool for estimating the power spectrum. We made a single realization of a “white” power spectrum sky (equal power on all scales) and then simulated the BEAST pipeline over that map. We created a full sky map with normally distributed noise in each pixel. This map was then smoothed with a Gaussian of  $\text{FWHM} = 23'$  to simulate our effective beam. Next we simulated the time-ordered data expected from this map without additional noise by sampling with the BEAST pointing timestream for a single day’s data. We ran the resulting timeline through the BEAST analysis pipeline, including template removal, filtering and binning. Finally, we cut using the same foreground template used in the actual data map. “pseudo- $C_l$ ” power spectra (that is power spectra calculated assuming full sky coverage but actually covering only a particular region) were calculated for the full unsmoothed white input map, the smoothed white map, the smoothed and foreground cut white map, and the full BEAST simulated smoothed and foreground cut map. The results are shown in Figure 10. The two all-sky power spectra have been scaled by the sky fraction (4% of full sky) of the foreground cut template in order to put them on scale and to demonstrate that the primary effect of limited sky coverage on our  $\ell$ -space filter is

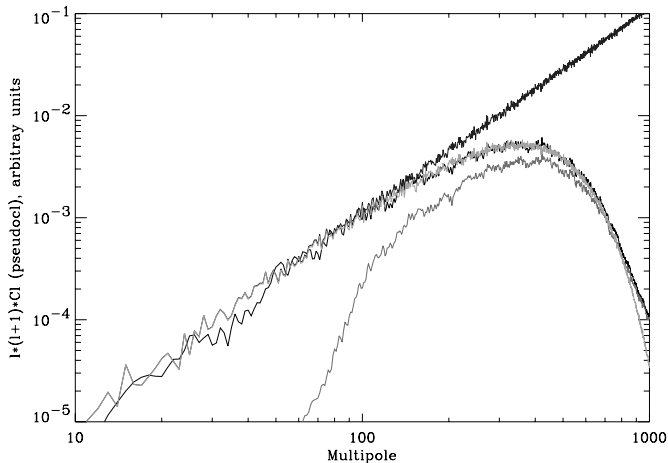


FIG. 10.—Approximate  $l$ -space description of the effective filtering produced by our pipeline processing and Galaxy cuts. Starting at the top: power spectrum for the full “white” simulated sky, scaled by the sky fraction; spectrum for 23’ FWHM smoothed simulation, scaled by sky fraction; 23’ smoothed simulation cut by Galaxy removal and BEAST sky coverage template; and smoothed sky simulation measured through BEAST pipeline analysis (no noise added). Note that all spectra were calculated using the HEALPix ANAFEST routine. Also all except the full sky spectrum are pseudo- $C_l$  spectra, calculated from partial sky coverage without any corrections. See the text for discussion. [See the electronic edition of the Supplement for a color version of this figure.]

just amplitude. All of the smoothed maps display the high  $l$  cutoff of our beam. Below  $l$  of about 150, the input map power spectrum is virtually the same as the smoothed and cut sky power spectra, while the BEAST simulated map power spectrum displays the low  $l$  cutoff of the combined template removal and 10 Hz high-pass filter. The loss of sensitivity from  $l \approx 50$  to  $l \approx 150$  is dominated by the high-pass filter cutoff. Following the same reasoning as the MASTER technique, we can generate a (rough) transfer function from the ratio of the pseudo- $C_l$  power spectrum of the full (noiseless) white-noise sky BEAST simulation to the input power spectrum. This is similar to a single “signal simulation.” This transfer function is rough, in that we have not explicitly taken the  $l$ - $l$  correlations created by the cut sky into account, and our use of a white-noise sky model may slightly bias the result.

In order to estimate the actual CMB power spectrum, even with our experimental filtering known, we need a very good estimate of the noise contribution as a function of  $l$ . One way to do this is via Monte Carlo simulations (e.g., MASTER), as are done in O’Dwyer et al. (2005). A second way to estimate the noise is to use a jackknife technique, where we generate two maps, one from the first half of the data and one from the second half. These maps should be independent measurements of the CMB sky, with correlated signal and uncorrelated noise. By taking a simple weighted difference of the maps we get a reasonable estimate of the instrument (and atmospheric) noise contributions, all weighted by the analysis filters. Calculating pseudo- $C_l$  power spectrum for this difference map, we can then subtract it from the normal data map pseudo- $C_l$  power spectrum to obtain the “true” signal pseudo- $C_l$ . Using the transfer function described above, we then estimate the actual sky power spectrum, which is displayed in Figure 11, along with the real spectrum calculated in O’Dwyer et al. and the “best-fit” theory spectrum of Bennett et al. (2003). Although this technique does not provide error bars, it is in reasonable agreement with the full analysis. This crude tool takes only minutes to run on a desktop computer and was invaluable in decipher-

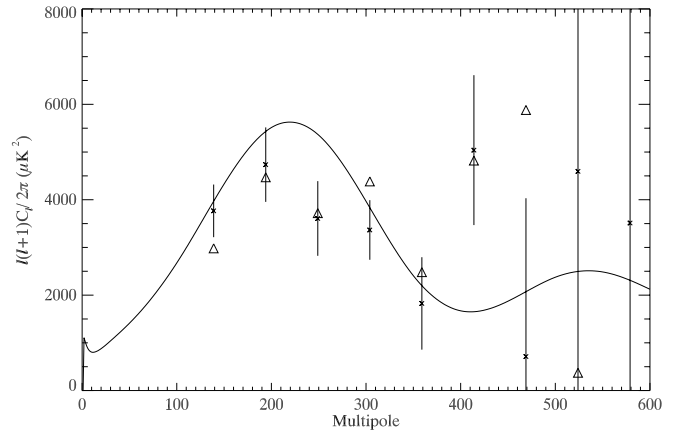


FIG. 11.—Comparison of the power spectra obtained using our “poor man’s” analysis method (open triangles) to the full MASTER implementation of O’Dwyer et al. (asterisks with error bars). The power spectrum of the WMAP “best-fit” theory model from Bennett et al. is shown as a smooth curve for reference. We obtain a reasonable estimate of the power spectrum at very low computing cost, at the expense of error estimates.

ing the dependence of our large data set on various cuts and adjustments.

#### 4. FUTURE OBSERVATIONS

We have shown the utility of making large area sky maps with a simple scanning strategy and could add significantly more data in the future. The data presented so far are the result of 27 days of “good data.” Our experience so far is that we can achieve good data on more than 50% of the days at our observatory. The site has proven to be extremely good in our wavelength range and the atmosphere stable. One year of observations with the existing system only improved by new HEMTs could yield 7  $\mu$ K errors per 30’ pixel on 10% of the sky. The BEAST optics are precise enough to observe to nearly 1 THz, so a variety of sky surveys are possible. At 90 GHz the beam size would be about 8.5 FWHM, while at 150 GHz it is 5’.

It is a pleasure to thank K. Gorski, D. Maino, D. Finkbeiner, S. Myers, T. Montroy, and J. R. Bond, for useful discussions. M. Lim and J. Staren made significant contributions early in the development of BEAST. We wish to thank the White Mountain Research Station, particularly D. Trydahl, R. Masters, and M. Morrison, for heroic efforts in getting BEAST sited. WMRS director F. Powell’s enthusiastic support has been critical to our success. BEAST was built with help from numerous talented UCSB physics undergraduates, as well as the superb UCSB machine shop, and administrative staff. We wish to thank E. Mattaini and E. Santambrogio from IASF Milano. We also want to thank the National Scientific Balloon Facility staff for their support on our two balloon campaigns leading up to the current ground-based work. The development and operations of BEAST were supported by NASA grants NAG5-4078, NAG5-9073, and NAG5-4185, and by National Science Foundation grants 9813920 and 0118297. In addition we were supported by the White Mountain Research Station, the California Space Institute (CalSpace), and the UCSB Office of Research. Production of the superb BEAST optics were made possible by personal and corporate support from K. Kedward (UCSB ME), M. Pryor (COI), S. Dummer (Surface Optics), J. Wafer and T. Ives (Thin Film Technology), TRW, J. Anthony (Union Carbide),

and Able Engineering. We had support from NRAO and M. Pospieszalski, as well as TRW in developing our HEMT amplifiers. N. F. and A. P. were partially supported by CNPq grant 470531/2001-0. J. M. is supported by FAPESP grants 01/13235-9 and 02/04871-1. T. V. and C. A. W. were partially supported by FAPESP grant 00/06770-2. T. V. was partially

supported by CNPq grants 466184/00-0 and 302266/88-7-FA. C. A. W. was partially supported by CNPq grant 300409/97-4 and FAPESP grant 96/06501-4. The research described in this paper was performed in part at the Jet Propulsion Laboratory, California Institute of Technology, under a contract with the National Aeronautics and Space Administration.

## REFERENCES

- Bennett, C. L., et al. 1992, *ApJ*, 396, L7  
 ———. 2003, *ApJS*, 148, 1  
 Benoit, A., et al. 2002, *A&A*, 399, L19  
 Bersanelli, M., Maino, D., & Mennella, D. 2002, *Nuovo Cimento Rivista*, 25, 1  
 Bond, J. R., & Efstathiou, G. 1987, *MNRAS*, 226, 655  
 Childers, J., et al. 2005, *ApJS*, 158, 124  
 De Bernardis, P., et al. 2000, *Nature*, 404, 955  
 Dennison, B., Simonetti, J. H., & Topasna, G. 1998, *Publ. Astron. Soc. Australia*, 15, 147  
 Figueiredo, N., et al. 2005, *ApJS*, 158, 118  
 Finkbeiner, D. P. 2003, *ApJS*, 146, 407  
 Gaustad, J. E., McCullough, P. R., Rosing, W. & Van Buren, D. 2001, *PASP*, 113, 1326  
 Gorski, K., et al. 1996, *ApJ*, 464, L11  
 Górski, K. M., Hivon, E., & Wandelt, B. D. 1998, in *Proc. MPA/ESO Conf. on Evolution of Large-Scale Structure: from Recombination to Garching*, ed. A. J. Banday, R. K. Sheth, & L. Da Costa (Garching: ESO), in press (astro-ph/9812350)  
 Halverson, N. W., et al. 2002, *ApJ*, 568, 38  
 Hivon, E., et al. 2002, *ApJ*, 567, 2  
 Hu W., & Dodelson, S. 2002, *ARA&A*, 40, 171  
 Kuo, C., et al. 2004, *ApJ*, 600, 32  
 Lee, A., et al. 2001, *ApJ*, 561, L1  
 Mason, B. S., et al. 2003, *ApJ*, 591, 540  
 Mejia, J., et al. 2005, *ApJS*, 158, 109  
 Netterfield, C. B., et al. 2002, *ApJ*, 571, 604  
 O'Dwyer, I., et al. 2005, *ApJS*, 158, 93  
 Reynolds, R. J., Haffner, L. M., & Madsen, G. J. 2002, in *ASP Conf. Ser. 282, Galaxies the Third Dimension*, ed. M. Rosado, L. Binette, & L. Arias (San Francisco: ASP), 31  
 Schlegel, D. J., Finkbeiner, D. P., & Davis, M. 1998, *ApJ*, 500, 525  
 Spergel, D., et al. 2003, *ApJS*, 148, 175  
 Staren, J., et al. 2000, *ApJ*, 539, 52  
 Tegmark, M., et al. 2000, *ApJ*, 541, 535